FUN3D Airload Predictions for the Full-Scale
UH-60A Airloads Rotor in a Wind Tunnel

Elizabeth M. Lee-Rausch
e.lee-rausch@nasa.gov
Research Engineer
NASA Langley Research Center
Hampton, Virginia, US

Robert T. Biedron
robert.t.biedron@nasa.gov
Senior Research Scientist
NASA Langley Research Center
Hampton, Virginia, US

ABSTRACT

An unsteady Reynolds-Averaged Navier-Stokes solver for unstructured grids, FUN3D, is used to compute the rotor performance and airloads of the UH-60A Airloads Rotor in the National Full-Scale Aerodynamic Complex (NFAC) 40- by 80-foot Wind Tunnel. The flow solver is loosely coupled to a rotorcraft comprehensive code, CAMRAD-II, to account for trim and aeroelastic deflections. Computations are made for the 1-g level flight speed-sweep test conditions with the airloads rotor installed on the NFAC Large Rotor Test Apparatus (LRTA) and in the 40- by 80-ft wind tunnel to determine the influence of the test stand and wind-tunnel walls on the rotor performance and airloads. Detailed comparisons are made between the results of the CFD/CSD simulations and the wind tunnel measurements. The computed trends in solidity-weighted propulsive force and power coefficient match the experimental trends over the range of advance ratios and are comparable to previously published results. Rotor performance and sectional airloads show little sensitivity to the modeling of the wind-tunnel walls, which indicates that the rotor shaft-angle correction adequately compensates for the wall influence up to an advance ratio of 0.37. Sensitivity of the rotor performance and sectional airloads to the modeling of the rotor with the LRTA body/hub increases with advance ratio. The inclusion of the LRTA in the simulation slightly improves the comparison of rotor propulsive force between the computation and wind tunnel data but does not resolve the difference in the rotor power predictions at $\mu = 0.37$. Despite a more precise knowledge of the rotor trim loads and flight condition, the level of comparison between the computed and measured sectional airloads/pressures at an advance ratio of 0.37 is comparable to the results previously published for the high-speed flight test condition.

NOTATION

a_∞ freestream speed of sound [ft/s]

c section blade chord [ft]

C_{Mx} hub rolling moment coefficient $\left(\frac{Mx}{\rho_\infty V_{tip}{}^2 \pi R^3}\right)$

C_{My} hub pitching moment coefficient $\left(\frac{My}{\rho_\infty V_{tip}{}^2 \pi R^3}\right)$

C_P rotor power coefficient $\left(\frac{P}{\rho_\infty V_{tip}{}^2 \pi R^2}\right)$

C_T rotor thrust coefficient $\left(\frac{T}{\rho_\infty V_{tip}{}^2 \pi R^2}\right)$

C_X rotor propulsive force coefficient $\left(\frac{X}{\rho_\infty V_{tip}{}^2 \pi R^2}\right)$

f_n sectional normal force [lbf/ft]

f_c sectional chord force [lbf/ft]

m $c/4$ sectional pitching moment [ft-lbf/ft]

M section Mach number

$M^2 C_c$ sectional chord force coefficient $\left(\frac{f_c}{\frac{1}{2}\rho_\infty a_\infty{}^2 c}\right)$

$M^2 C_m$ $c/4$ sectional pitching moment coefficient $\left(\frac{m}{\frac{1}{2}\rho_\infty a_\infty{}^2 c^2}\right)$

$M^2 C_n$ sectional normal force coefficient $\left(\frac{f_n}{\frac{1}{2}\rho_\infty a_\infty{}^2 c}\right)$

M_x rotor hub rolling moment [ft-lbf]

M_y rotor hub pitching moment [ft-lbf]

P rotor power [ft-lbf/s]

r radial position [ft]

R rotor radius [ft]

T rotor thrust [lbf]

V velocity [ft/s]

x chordwise distance from leading edge [ft]

X rotor propulsive force [lbf]

α_c corrected shaft angle [°]

α_s geometric shaft angle [°]

μ advance ratio $\left(\frac{V_\infty}{V_{tip}}\right)$

ρ_∞ freestream density [slugs/ft^3]

σ solidity

ψ azimuthal position [°]

$()_{tip}$ denotes blade tip

$()_\infty$ denotes freestream condition

INTRODUCTION

The flight test of the UH-60A airloads rotor in 1993 provided an extensive database for the validation of predictive analy-

sis tools (Refs. 1, 2). Numerous studies have been published that compare loosely-coupled Computational Fluid Dynamics (CFD) and Computational Structural Dynamics (CSD) predictions with the flight test data. The use of CFD has typically shown improved comparison of airloads between flight test and computation compared to the lower-fidelity models available in CSD comprehensive codes. Despite a high level of fidelity in aerodynamic modeling (including Reynolds-Averaged Navier-Stokes (RANS) and Detached-Eddy Simulations (DES)) and a high level of spatial/temporal resolution, the correlation of the predicted and measured airloads has appeared to reach a plateau (Refs. 3–5). Differences in sectional airloads between the various simulations are in general smaller than the difference between the simulations and flight data. In particular, computed sectional pitching moments and chord forces often exhibits a significant mean-value offset from flight, and the computed sectional chord force exhibits significant differences from flight on the advancing side of the rotor. The current authors showed that computed chord force results compare more favorably with flight test data when a consistent integration method is used between the CFD and flight, but the computed sectional normal force and pitching moment results were not very sensitive to the integration method (Ref. 6). Reference 6 also presented a comparison of chordwise pressure distributions between computation and flight that highlighted the modeling of individual flow features such as shocks and leading-edge vortices. In particular at the high speed flight condition (C8534), the computed shock locations on the advancing side of the rotor are farther forward and slightly weaker than in the test data.

There are many possible reasons for discrepancies between flight and computation due to the need to account for aerodynamics, structural dynamics, and trim. Also, due to the nature of flight testing, some important information is either not available from flight or can only be estimated. For example, main rotor thrust was determined from estimates of vehicle weight, downwash loading on the fuselage, and tail rotor loading at a particular flight condition. A full-scale wind-tunnel test of the same UH-60A airloads rotor was completed in 2010 at the National Full-Scale Aerodynamic Complex (NFAC) 40-by 80-foot Wind Tunnel (Ref. 7). The wind-tunnel test provided an opportunity to test the airloads rotor in a more controlled environment without the influence of a tail rotor or propulsion system. (However, testing in a facility requires accounting for the influence of tunnel blockage, wall interference, and other flowfield non-uniformities.) The wind-tunnel test also produced additional data not available from the flight test including new measurements and additional flight/trim conditions. The new measurements include rotor hub forces and moments, oscillatory hub loads, blade displacements and deformations, and rotor wake measurements.

Comparisons between the new wind-tunnel data and CFD/CSD simulations have begun (Refs. 8–12). Romander et al. (Ref. 8) performed loosely-coupled OVERFLOW 2/CAMRAD-II analyses of the isolated rotor and made initial comparisons with integrated performance loads and sectional airloads from the NFAC test. Results presented in Ref. 8 showed reasonable agreement with the trends in measured aerodynamic loads and in the sectional airloads for a 1-g level flight speed sweep and a parametric thrust sweep. However, discrepancies in the mean sectional pitching moment and chord force magnitudes were noted. Initial comparisons of experimental and computational blade displacements for the same OVERFLOW 2/CAMRAD-II loosely-coupled analyses were shown in Ref. 9. For a moderate advance ratio, the comparisons show good trend agreements, but also indicate significant discrepancies in mean lag and elastic twist. Blade displacement pitch measurements agreed well with both the wind tunnel commanded and measured values. Yeo and Romander (Ref. 10) have also shown comparisons of CAMRAD-II and OVERFLOW 2/CAMRAD-II oscillatory structural load predictions with the NFAC data. In general, the oscillatory structural loads predictions were improved with the coupled CFD/CSD analysis, but the chord bending moment was still significantly under-predicted. Marpu et al. (Ref. 12) performed loosely-coupled CFD/CSD analyses of the isolated rotor with a hybrid Navier-Stokes/free-wake CFD code (GT-Hybrid) coupled with a multi-body dynamics analysis code (DYMORE). Results presented in Ref. 12 showed reasonable agreement between measured and predicted integrated performance loads for a speed and thrust sweep but also noted an underprediction of chord bending moments. References 8 and 11 showed sensitivity of the sectional airloads to tunnel wall and test stand modeling but noted that increased geometric fidelity did not resolve the airloads discrepancies between computation and experiment.

In the current study, simulations of the UH-60A airloads rotor in the NFAC facility are made with the FUN3D CFD code loosely-coupled to the CAMRAD-II CSD code. FUN3D, an unstructured-grid RANS solver, and CAMRAD-II have previously been used to simulate the UH-60A Airloads flight test configuration (Refs. 3, 6). These loosely-coupled FUN3D/CAMRAD-II airloads results for the isolated rotor compared closely with other state-of-the-art methods (Ref. 4). The same FUN3D/CAMRAD-II rotor models are used in this study for a detailed analysis of the UH-60A Airloads Wind Tunnel speed sweep test conditions. Isolated rotor analyses are shown to provide comparisons with the isolated rotor analyses of the flight-test configuration and the recent OVERFLOW 2/CAMRAD-II computations by Romander et al. (Ref. 8). Computations with the airloads rotor installed on the NFAC Large Rotor Test Apparatus (LRTA) and in the 40- by 80-ft wind tunnel are also shown to illustrate the influence of the test stand and wind-tunnel walls on the rotor performance and airloads. Rotor trim tab deflections are also included in the model to determine their effect on rotor performance and airloads. Detailed comparisons are made between the results of the CFD/CSD simulations and a number of the wind tunnel measurements: rotor trim loads and trim control angles, rotor performance loads, rotor sectional loads, and blade pressures. The process described in Ref. 6 is also used to determine the sensitivity of the computed sectional loads to the integration method.

UH-60A AIRLOADS WIND TUNNEL TEST

In 2010, a full-scale wind-tunnel test of the UH-60A airloads rotor was conducted at the NFAC 40- by 80-foot Wind Tunnel (Ref. 7). Figure 1 shows the airloads rotor mounted on the LRTA in the NFAC. The primary objective of the test was to acquire a comprehensive set of validation-quality measurements on a full-scale rotor at challenging conditions outside the conventional flight envelope. A secondary objective of the test was to provide data to evaluate the similarities and differences between small-scale wind tunnel, full-scale wind tunnel, and full-scale flight test. To meet these objectives, the test was separated into six phases: (1) 1-g level flight speed sweeps, (2) parametric sweeps, (3) Airloads flight test simulations, (4) small-scale wind tunnel test simulations, (5) high advance ratio (slowed rotor) testing, and (6) particle image velocimetry (PIV) testing.

Fig. 1. UH-60A Airloads Rotor mounted on the LRTA in the NFAC 40- by 80-foot Wind Tunnel.

To provide an expanded database for predictive tools, an extensive set of measurements were made during the test. As in the flight-test campaign, one blade was instrumented with unsteady pressure transducers, and a second blade was instrumented with strain gages and accelerometers. The wind-tunnel test also produced additional data not available from the flight test including rotor hub forces and moments, oscillatory hub loads, blade displacements and deformations, and rotor wake measurements. The new measurements allow for a more precise knowledge of rotor flight and trim conditions. Currently, data are available from two of the test runs: a 1-g level flight sweep (Run 52) and a parametric thrust sweep (Run 45). (Note that rotor deformation and wake measurement were not taken at these test points.) The speed sweep (Run 52) is the focus of this paper.

For the speed-sweep test conditions, shaft angle and trim targets were allowed to vary across the speed range to achieve the target rotor lift and propulsive targets expected to occur in flight. The speed sweep (Run 52) was conducted at a constant solidity-weighted lift coefficient of 0.0902 over a range

of advance ratios from $\mu = 0.15$ to 0.40 with a (hover) tip Mach number of $M_{tip} = 0.65$. In this study, comparisons will be made between the results of the CFD/CSD simulations and wind-tunnel test measurements of rotor trim loads, trim control angles, rotor performance loads, rotor sectional loads, and blade pressures. Table 1 summarizes the trim conditions for the data points in Run 52. Wall corrections in the form of an induced angle-of-attack correction were calculated using the Prandtl-Glauert equations. The correction term was added to the geometric rotor shaft angle (α_s). The corrected shaft angle of attack (α_c) was used to compute the rotor lift and propulsive forces. Additionally, aerodynamic tares were subtracted from the rotor balance loads to compensate for hub/shaft/control system loads. Two independent systems were used to measure blade flap, lag, and pitch angles at the root of each blade. However at the time of publication, the post-test data validation for these measurements was not complete (Ref. 13).

Table 1. Run 52 speed sweep trim conditions.

Point	μ	C_T/σ	α_s (°)	α_c (°)
15	0.15	0.902	-1.90	0.89
20	0.20	0.902	-1.90	-0.31
25	0.24	0.903	-2.60	-1.50
31	0.30	0.905	-4.20	-3.40
35	0.35	0.906	-6.10	-5.58
40	0.37	0.907	-7.20	-6.74
46	0.39	0.908	-8.00	-7.57
51	0.40	0.907	-8.00	-7.60

One blade of the airloads rotor was instrumented with 241 unsteady pressure transducers. Transducers were generally grouped chordwise along nine radial stations. Figure 2 shows the radial stations at which test data were collected. A maximum of 15 transducers were installed on the upper-surface at each radial station, along with a maximum of 15 transducers on the lower-surface at each station. As in the flight-test program, the blade pressures were integrated to provide normal force, pitching moment, and chord force for each radial station. Although the transducers were clustered near the leading edge to better resolve the pressure distribution there, the number of points used to integrate the measured data were sparse in comparison with the number of points typically used for integration of CFD data. Furthermore, not all transducers remained operational for all of the run conditions of the test program. Aerodynamic shear stresses were not measured, so the experimental integrated sectional airloads reflect only the pressure contribution. For Run 52, there was not a sufficient number of operational pressure transducers to provide sectional airloads for station $r/R = 0.550$. Also, the airloads stations at $r/R = 0.675$, 0.965, and 0.990 had a small number (7–8) of operational transducers on one side of the blade. Reference 7 gives a detailed description of the test hardware, instrumentation, and data reduction. The wind tunnel test conditions and data shown in this work were provided by the Airloads Wind Tunnel Test team.
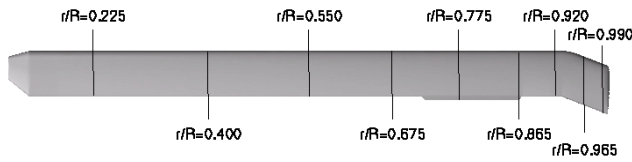
Fig. 2. UH-60A Airloads Rotor pressure transducer radial locations.

CFD/CSD METHODOLOGY

The unstructured-grid flow solver used for this study is FUN3D (Ref. 14). The code solves the unsteady Reynolds-Averaged Navier-Stokes equations, with several models available for turbulence closure. The solver has a variety of mesh-motion options, including rigid, deforming, and overset meshes, and a robust implicit time-advancement scheme. For overset meshes, the DiRTlib (Ref. 15) and SUGGAR++ (Ref. 16) codes are used to facilitate communication between disparate zones in the mesh. Aeroelastic effects and trim are accounted for via coupling with a rotorcraft comprehensive code, CAMRAD-II (Ref. 17).

The aerodynamics modules within CAMRAD-II are based on lifting-line models utilizing airfoil tables, coupled with wake models. Although such aerodynamic models can provide reasonable results for many flight conditions, in some cases the predictions of the airloads can be inaccurate because of limitations of the relatively low-order aerodynamic modeling. When converged, the loose coupling approach replaces the low-order lifting-line aerodynamics of the CSD code with the higher-fidelity Navier-Stokes aerodynamics of the CFD code. Within CAMRAD-II, each blade is modeled as a set of nonlinear beam elements. In addition to the structural dynamics modeling, CAMRAD-II offers a sophisticated trim capability.

The coupling is implemented via a loose coupling strategy, which is appropriate for steady, level flight. The rotor aerodynamic loads are not exactly conserved between the CSD and CFD analyses in the loose-coupling process with CAMRAD-II. One reason is that only 3 of the 6 sectional forces are transferred to the CAMRAD-II model: normal force, pitching moment, and chord force. Also, the CSD and CFD models have different spatial and temporal resolutions. Matching the model resolutions does improve the loads conservation. A full description of the CFD method and coupling strategy can be found in Ref. 3. For the UH-60A speed sweep, a three-degree-of-freedom trim is utilized, with the (solidity-weighted) thrust coefficient, pitching moment, and rolling moment specified as trim targets within CAMRAD-II. The free-air simulations use the corrected shaft angle while the simulations with the tunnel walls use the uncorrected shaft angle.

MODELS

CSD Structural Model

The current simulations use the CAMRAD-II structural model from Ref. 3. However, based on the recommendation of Ro-

mander (Ref. 18), some small changes have been made in the CAMRAD-II analysis to improve the resolution of data transfer between the CFD and CSD models in the loose-coupling process. The number of radial aerodynamic panels in the CAMRAD-II model has been increased from 21 to 100. Also, the azimuthal resolution of CAMRAD-II has been increased from 24 to 360 steps per revolution to match the CFD resolution.

CFD Aerodynamic Model

In order to study the influence of the test stand and wind tunnel walls, three different composite grids were developed for the three different aerodynamic configurations: (1) the isolated rotor in free air, (2) the rotor with LRTA/notional hub in free air, and (3) the rotor with the LRTA/notional hub in the tunnel. The composite grid for each configuration was developed by over-setting component grids for each individual blade with the appropriate background grid. A detailed discuss of each component grid is included the in the following subsections. The direct-cut method was used to define the blanked points in the composite grid, and an overlap minimization process was used to identify fringe points. A donor quality value of 0.9 was specified, and small number of orphans (less than 400) were generated in the overlap process.

The component unstructured grids for the overset computations were generated with the VGRID v4.0 advancing-layer and advancing-front grid generation software package (Ref. 19). The grid cells near the blade and LRTA surfaces are prismatic in shape, and transition to tetrahedra away from the surface. The component blade grids and isolated rotor background grid used in this study are the same as used in Refs. 3 and 6 to analyze the flight-test conditions. A time step corresponding to $1°$ change in rotor azimuth was used for the CFD computations, and the Spalart-Allmaras turbulence model was employed to model the effects of turbulence. Further details of the isolated rotor numerical simulations, as well as an examination of the sensitivity of the results to mesh size, time step, and turbulence model are available in Ref. 3 where sectional airloads (normal force, pitching moment, and chord force) were found to be insensitive to the aforementioned parameters.

Blade Grid The blade surface geometry used for grid generation is based on an updated definition provided by the Sikorsky Aircraft Corporation via the UH-60 Airloads Workshop in May 2009. Figure 2 shows the surface definition of the blade grid. Note that no surface geometry was provided inboard of the $r/R = 0.13$ station so the CFD surface grid is approximate inboard of that station. The near-body blade grid extends away from the blade to a cylindrical outer boundary of radius $1.5c_{tip}$. In the wall normal direction, the grid spacing is set such that an average normalized coordinate y^+ is less than one for the first grid cell at the wall for the majority of the blade. A no-slip boundary condition is applied at the blade surface. The characteristic spacings of the blade surface grid are summarized in Ref. 3. The maximum spacing at

the blade grid outer boundary is approximately $0.10c_{tip}$. Each component blade grid has approximately 2.65 million nodes. The trim tab deflection, when included, is modeled by deforming the surface grid of the blade by the specified amount and adjusting the volume grid points with the deforming mesh algorithm. The measured tab deflection angles are $1.6°$, $2.0°$, $0.3°$, and $3.7°$ for blades 1–4, respectively. (Blade 1 has the pressure transducer measurements, and blade 3 has the strain gage measurements.) For the current study, a tab angle of $3.6°$ is applied to all blades to simulate the maximum effect.

Isolated Rotor Free-Air Grid The background grid for the isolated rotor in free air is a square box whose sides extend $5R$ out from the rotor hub. The finest spacing in the background grid is approximately $0.10c_{tip}$. This minimum spacing is maintained, within the constraints of the unstructured meshing software, in a cylindrical volume which extends $1.1R$ in the blade plane and $0.20R$ above and $0.20R$ below the blade plane. The background component grid has approximately 7.0 million nodes. The isolated-rotor composite grid has a total of approximately 17.6 million nodes. A freestream characteristic boundary condition is set on the outer boundaries of the background grid, and the corrected shaft angle is used for the free-air computations.

Rotor/LRTA Free-Air Grid The background grid for the LRTA body/hub is a single component grid. The LRTA is embedded in a square box whose sides extend $5R$ from the rotor hub. The LRTA surface geometry used for grid generation is based on a definition provided by the UH-60A Airloads Wind Tunnel Test team. A simplified notional hub was included in the CFD model to provide blockage in that area of the grid. The geometry of the notional hub was based on gross measurements/locations of the instrumentation hat and shaft diameter provided by the test team. Figure 3 shows the surface definition and surface grids for the blades, LRTA, and notional hub. The shaft, hub, and instrumentation hat do not rotate. The LRTA body/hub are modeled as viscous surfaces. In the wall normal direction, the grid spacing is set such that y^+ is less than one for the first grid cell at the wall for the majority of the body, and a no-slip boundary condition is applied at the blade surface. As with the isolated rotor background grid, there is a cylindrical volume of refinement where the component blade grids are overset with the LRTA background grid. The spacing in this cylindrical volume is the same as used for the free-air cases ($0.10c_{tip}$). The LRTA free-air background grid has 7.5 million nodes, and total composite mesh with blades contains approximately 18 million nodes. A freestream characteristic boundary condition is set on the outer boundaries of the background grid, and the corrected shaft angle is used for the free-air computations.

Rotor/LRTA in Tunnel Grid The background grid of the LRTA body/hub in the NFAC wind tunnel is also a single component grid. This grid uses the same LRTA body/hub geometry and surface grid spacings used in the LRTA free-air background grid. As a first effort to estimate the effects of the
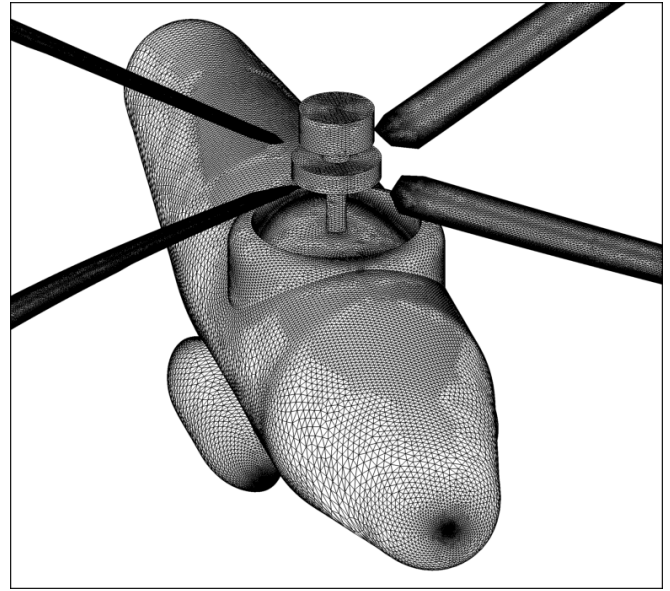

Fig. 3. CFD model of the UH-60A Airloads Rotor on the LRTA.

walls on rotor performance and sectional airloads, the tunnel geometry has been simplified. The tunnel walls are modeled as inviscid boundaries with a constant area cross-section that matches the cross-section at the entrance to the NFAC test section. The inflow and outflow boundaries are placed upstream and downstream of the rotor origin at one and half times the NFAC test section length (approximately $4.5R$). Figure 4 shows a portion of the tunnel surface grids and a volume cut from the unstructured-grid model of the LRTA in the simplified NFAC wind tunnel (viewed from downstream). As with the free-air background grids, there is a cylindrical volume of refinement ($0.10c_{tip}$) where the component blade grids are overset with the LRTA/tunnel grid. The crinkle-cut through the volume grid in Fig. 4 shows this refinement. At the tunnel inflow boundary, test-section flow conditions are specified with a Riemann boundary condition. At the outflow boundary, the mass and velocity variables are extrapolated, and the static pressure ratio is set to conserve mass flow through the computational tunnel. (The FUN3D actuator disk capability was used to quickly assess the static pressure ratio value needed to maintain the tunnel mass flow.) The LRTA/tunnel background grid has 7.5 million nodes, and total composite mesh with blades contains approximately 18 million nodes. The uncorrected shaft angles are used for the in-tunnel simulations. The LRTA angle of attack is set by deforming the surface grid of the body/hub by the specified amount and adjusting the volume grid points with a deforming mesh algorithm.

RESULTS

In this section, computational results are shown for wind-tunnel test conditions corresponding to a speed sweep at constant lift. The speed sweep (Run 52) was conducted at constant solidity-weighted lift coefficient of 0.0902 over a range of advance ratios from $\mu = 0.15$ to 0.40 with a (hover) tip
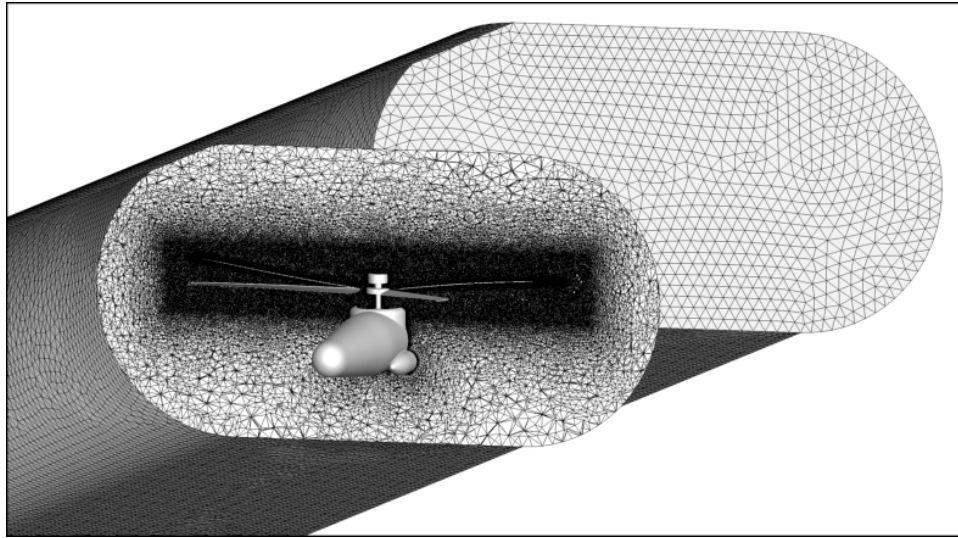
Fig. 4. Surface grids and volume cut from the CFD model of the LRTA in the simplified NFAC tunnel (viewed from downstream).

Mach number of $M_{tip} = 0.65$. Loosely-coupled CFD/CSD computational results from four different aerodynamic configurations are compared to the wind-tunnel data: (1) the isolated rotor in free air, (2) the rotor/LRTA in free air, (3) the rotor/LRTA with deflected trim tabs in free air, and (4) the rotor/LRTA in the tunnel. Isolated rotor computations were made at five of the eight advance ratios tested in Run 52: $\mu = 0.15, 0.20, 0.30, 0.37,$ and 0.40. Rotor/LRTA free-air and in-tunnel computations were made on a subset of these conditions: $\mu = 0.15, 0.30,$ and 0.37. Computations of the rotor/LRTA with deflected trim tabs in free air were only made at $\mu = 0.37$.

First, computational results are compared to the trim and performance data from the test to assess the sensitivity of the integrated rotor loads to advance ratio and aerodynamic configuration. Next, the rotor sectional loads are compared to the test data to assess the sensitivity of the rotor disk (distributed) loading to advance ratio and aerodynamic configuration. The influence of sectional load integration method are shown for a representative subset of the data. The interpretation of the sectional airload data can be greatly enhanced by comparing the computed and measured unsteady pressure distributions at each of the airloads stations. However, space constraints make it impractical to include a large number of comparisons in the paper. A subset of sectional pressures are shown to highlight discrepancies in the prediction of individual flow features.

Rotor Trim and Performance

Figure 5 shows comparisons of integrated rotor trim loads and control angles between test and computation. The test data are plotted with a mean and standard deviation. The mean value is a simple average of all data acquired during the data point (128 rotor revolutions), and the standard deviation is the standard deviation of the mean which is a measure of the variabil-

ity of the mean from revolution to revolution (not from sample to sample). The rotor pitching moment is positive nose up, and the rolling moment is positive starboard up. The computed loads are from the integration on the CFD mesh. As previously noted, the airloads are not conserved in the loose-coupling procedure so the CFD loads do not exactly match the trim targets in the CSD analysis (which match the test values to within plotting accuracy). The trim thrust values match to within 1 percent of the test values, and the trim moments match to within a few percent of the test data. The variation in fixed-system pitch control angles with advance ratio is well predicted. However, the trim collective pitch angle tends to be over-predicted by $1-1.5°$. The sensitivity of pitch trim to aerodynamic configuration is very small. There is some slight improvement to the comparison of longitudinal cyclic trim when the LRTA body is included in the computation. The computations show a similar sensitivity of flap and lag angles to aerodynamic configuration. The variation is less than $0.1°$. Although the computed control angles are well predicted, the prediction of the rotor dynamic trim state cannot be assessed without the blade-root motion measurements.

Figure 6 shows comparisons of integrated rotor power and propulsive force between test and computation. The test data is plotted with a mean and standard deviation which is computed similarly to the test data in Fig. 5. The free-air computations are compared to the wind-tunnel propulsive force computed with the corrected shaft angle, while the in-tunnel computations are compared to the wind-tunnel propulsive force computed with the uncorrected or geometric shaft angle. The computed trends in solidity-weighted propulsive force and power coefficient match the experimental trends over the range of advance ratios and are comparable to the results shown in Refs. 8 and 11. There is little sensitivity in rotor power prediction to the modeling of the LRTA body/hub. The power is under predicted at the high advance ratios (3.6%)
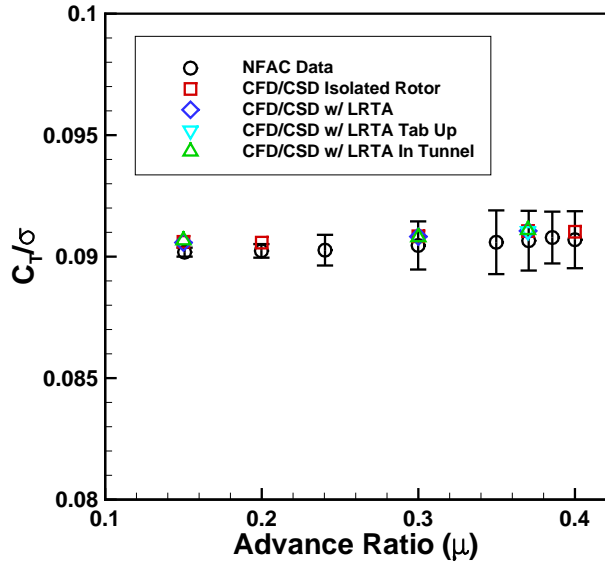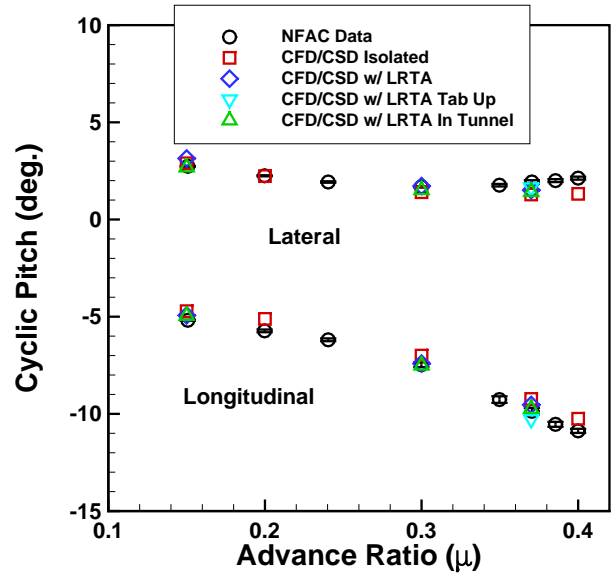
(a) Solidity-weighted thrust coefficient
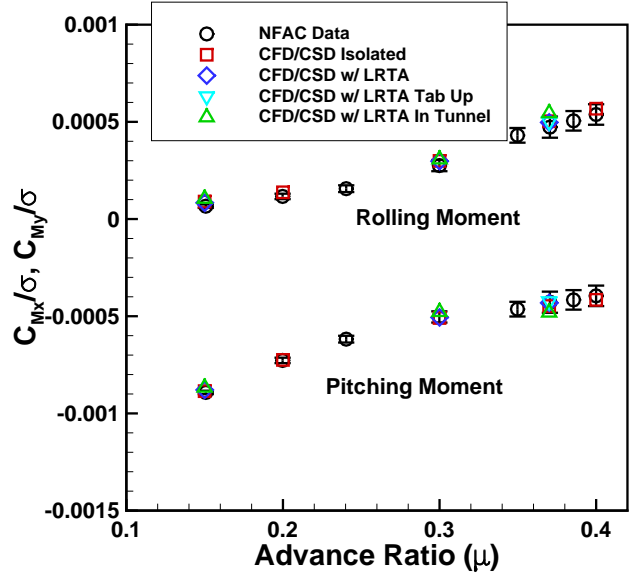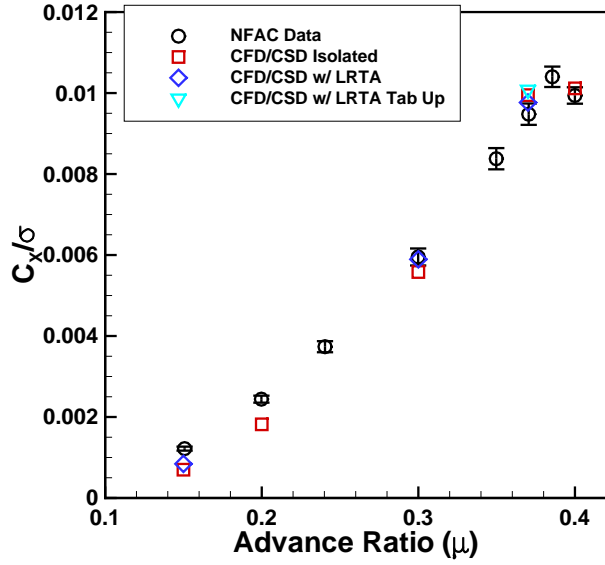
(b) Solidity-weighted moment coefficients
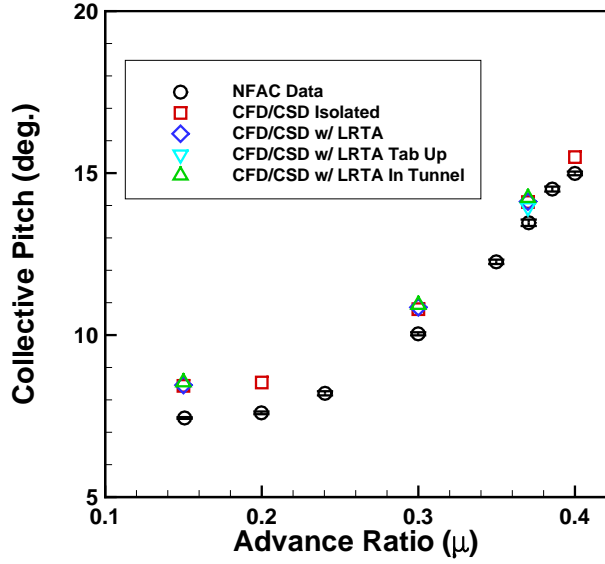
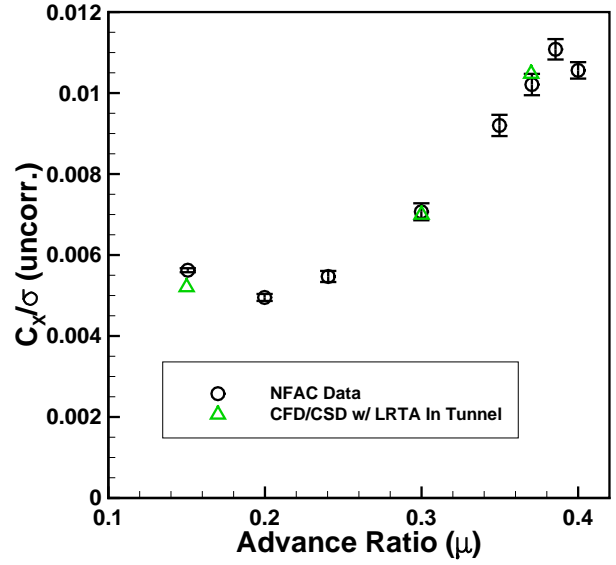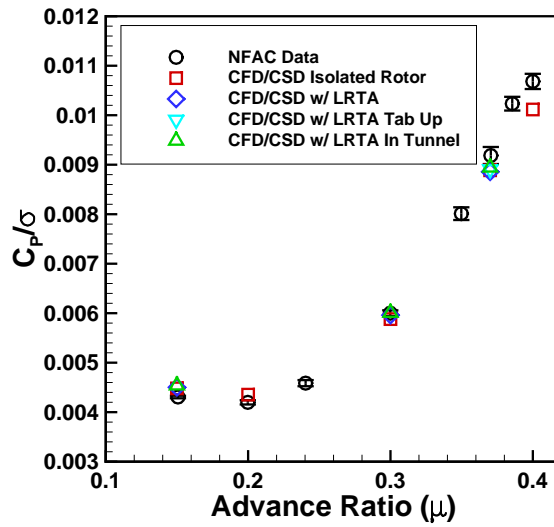**(c) Collective pitch angle**

(d) Cyclic pitch angles

Fig. 5. Rotor trim loads and control angles for speed sweep $\mu = 0.15 - 0.40$.

(a) Solidity-weighted propulsive force coefficient (corrected shaft angle)

(b) Solidity-weighted propulsive force coefficient (uncorrected shaft angle)

(c) Solidity-weighted power coefficient

Fig. 6. Rotor performance loads for speed sweep μ =0.15–0.40.

and over predicted at the low advance ratios (4.4%), but the power prediction at $\mu = 0.30$ matches the test data to within plotting accuracy (0.7%) when the LRTA is included in the CFD model. Overall, the addition of the LRTA body/hub to the CFD model improves the propulsive force predictions. The propulsive force is under predicted at the low advance ratios (30%) and slightly over predicted (3.1%) at the high advance ratios, but the propulsive force prediction at $\mu = 0.30$ matches the test data to within plotting accuracy (1.1%) when the LRTA is included in the CFD model. Overall, there is little sensitivity in rotor performance to the modeling of the wind-tunnel walls, nor does the deflection of the trim tabs significantly impact the performance of the rotor at $\mu = 0.37$.

Sectional Airloads – Polar Plots

The computed sectional force and moment coefficients are first presented in polar plot format to qualitatively assess the sensitivity of the rotor disk (distributed) loading to advance ratio and aerodynamic configuration. For the polar plots shown in Figs. 7–16, the sectional airloads are plotted around the rotor azimuth. (The results are all presented in the CFD reference frame, which has an azimuthal offset of 7 degrees from the wind tunnel data.) Generally at $\psi = 0°$, the blade is aligned with the freestream on the downstream side of the body, and at $\psi = 180°$, the blade is aligned with the freestream on the upstream side of the body. At $\psi = 90°$, the blade is perpendicular to the freestream on the advancing side of the rotor, and at $\psi = 90°$, the blade is perpendicular to freestream on the retreating side. The radial resolution of the plot is based on the 9 radial stations indicated in Fig. 2. Therefore, the data range is $r/R = 0.225$–0.990. The left-hand side of Figs. 7–15 shows the magnitude of sectional normal force, pitching moment and chord force for the isolated rotor in free air at $\mu = 0.15$, 0.30 and 0.37. (Pitching moment is positive nose up, chord force is positive directed toward the leading edge, and normal force is positive up.) The middle figures show the delta loading from the isolated rotor in free air to the rotor/LRTA in free air. The right figures show the delta loading from the rotor/LRTA in free air to the rotor/LRTA in the tunnel. Figure 16 shows the delta loading from the rotor/LRTA in free air with a nominal tab to the rotor/LRTA in free air with a deflected tab.

Overall, there is little sensitivity in rotor sectional airloads to the modeling of the wind-tunnel walls, which indicates that the shaft angle-of-attack corrections adequately compensate for the wall influence. Chang et al. (Ref. 11) made a similar conclusion regarding the wall corrections at and below $\mu = 0.37$ but showed an effect of wall modeling at a higher advance ratio ($\mu = 0.40$). Figures 7, 10, and 13 show that the inclusion of the LRTA body/hub does not have a significant impact on the sectional loads at $\mu = 0.15$. However, the inclusion of the LRTA body/hub does have a significant impact on the sectional normal forces at $\mu = 0.30$ and $\mu = 0.37$. Figures 8 and 9 show that the LRTA body/hub causes sectional normal force to increase inboard around $\psi = 180°$ and decrease outboard around $\psi = 0°$ and $\psi = 90$–$180°$. The inclusion of the LRTA body/hub also has a noticeable impact on

the sectional pitching moment and chord force at $\mu = 0.30$ and $\mu = 0.37$. Figures 11–15 show that the changes in sectional pitching moment and chord force are limited to the inboard station near $\psi = 180°$. More significant changes in the outboard sectional normal force and pitching moment are shown in Fig. 16 due to the deflection of the trim tabs. The trim tab imparts a nose-up pitching moment to the blade outboard on the advancing side of the rotor ($\psi = 0$–$180°$) and increases the normal force on the tip of the blade.

Sectional Airloads and Pressure Distributions

Before focusing on a more quantitative comparison between the computed and measured sectional airloads, the different methods used for the integration of the sectional airloads between the CFD and experiment are noted. In contrast to the integration of the measured sectional loads, which includes only pressure contributions, the integration of the CFD solution includes both pressure and shear-stress contributions. The CFD integration also includes a much higher spatial resolution at each radial location (approximately 250 mesh points versus a maximum of 30 pressure ports). To allow for a direct comparison with the measured-data integration, the CFD data (pressure only) from FUN3D can be processed in exactly the same manner as the wind-tunnel test data so that only the valid tap locations are used. This is done by interpolating the CFD data to the pressure tap locations and processing the CFD data through the same interpolation software as used for the test data, the TRCPCL code (Ref. 20).

Since one objective of this section is to show the sensitivity of the CFD solution to advance ratio and aerodynamic configuration, the majority of the computational sectional loads presented are computed with the full-resolution CFD integration method. However, the influence of sectional load integration method is shown in Figure 17 for the rotor with LRTA body/hub at the $\mu = 0.37$ advance ratio. Figure 17 compares the full-resolution CFD integration and the TRCPCL integration to the test data at a subset of the airloads stations: $r/R = 0.225$, 0.675, 0.920, and 0.990. The test data is plotted with an average and standard deviation time history. The average time history is an ensemble average over the entire data point (128 rotor revolutions). The standard deviation time history is a single revolution of data where each sample is the standard deviation at a single azimuth position computed over the entire data point. This provides a measure of the variability of the test data as a function of azimuth position. There is little sensitivity between the CFD method of integration and the TRCPCL method for the normal force and pitching moment except at stations $r/R = 0.675$ and 0.990 where there is a small number of operational transducers. The effect is particularly significant in the first quadrant of $r/R = 0.990$ where the loss of pressure transducers leaves a gap on the upper surface between $x/c = 0.11$ and 0.45 of the local chord. (A similar sensitivity is also seen at station $r/R = 0.965$ where there is also a small number of operational transducers.) Sectional chord force does show a significant effect from the integration method at all the stations, particularly on the advancing side

of the rotor disk. The computed chord force results compare more closely with test when a consistent method of integration is used. The sensitivity of computed sectional load integration method shown in Figure 17 is similar to results shown in Ref. 6.

Figures 18 - 21 compare the full-resolution CFD sectional airloads to the test data for a subset of the airloads stations: r/R= 0.225, 0.675, and 0.920. Figures 18 - 20 show the sensitivity to LRTA and tunnel wall modeling for μ =0.15, 0.30, and 0.37, respectively. Figure 21 shows the sensitivity to tab deflection for $\mu = 0.37$. The overall level of comparison between computed and measured sectional airloads is comparable to the results shown in Refs. 8 and 11.

At $\mu = 0.15$ (Fig. 18), the overall levels and trends in sectional normal force are well predicted including the blade-vortex interaction at the outboard station $r/R = 0.920$. Note that at this low advance ratio, there is no indication of shock formation on the advancing side of the rotor. The level of computed sectional pitching moment at the two inboard stations is more positive (nose up) than the test. The sectional pressures at these stations show that the CFD/CSD tends to overpredict the leading-edge suction peak on the upper surface of the blade in comparison with the test data. At the outboard station, the computed pitching moment compares more closely to the data on the advancing side, but the level is more negative on the retreating side. The sectional pressures at r/R =0.920 show that the CFD/CSD tends to underpredict the leading-edge suction on the upper surface of the blade in comparison with the test data. The computed chord force is well predicted at r/R= 0.225, but at the outboard stations chord force exhibits an offset on the advancing side which can be partially attributed to the integration method. The variation in the computed sectional loads due the LRTA and tunnel wall modeling is generally small in comparison to the revolution-to-revolution variation in the test data.

The sectional loads for the higher advance ratios $\mu = 0.30$ and 0.37 are shown in Figs. 19 and 20, respectively. Figures 22–24 shows the corresponding sectional pressure distributions at $\mu = 0.37$ advance ratio. The computed sectional pressure distributions are from the free-air simulations of the rotor with the LRTA body/hub. Sectional pressures are shown from the r/R= 0.225, 0.675, and 0.920 sections on the advancing and retreating side at $\Delta\psi = 45°$ increments. Note that at the higher advance ratios, strong shocks form outboard on the upper and lower surfaces of the blade on the advancing side of the rotor. The overall levels and trends in sectional normal force are well predicted. However, the inclusion of the LRTA in the computation tends to shift the peak values of normal force away from the test data in the second and third quadrant. The level of computed sectional pitching moment at the two inboard stations is generally more positive (nose up) than the test data due to a tendency of the CFD/CSD to overpredict the leading-edge suction peak on the upper surface of the blade. At $\mu = 0.30$, the computed pitching moment at r/R =0.920 compares more closely to the test data on the advancing side, but the level is too negative on the retreating side. The sectional pressures at at this station show that the CFD/CSD tends

to underpredict the leading-edge suction on the upper surface of the blade in comparison with the test data especially on the retreating side. Despite the good comparison of pitching moment levels on the advancing side, the simulation predicts weaker shocks that are located forward of the test data. For $\mu = 0.37$, similar discrepancies are seen at r/R =0.920 between the computed sectional pressures and test data resulting in an underprediction and overprediction of the pitching moment. As previously shown in Fig. 17, the computed chord forces likely exhibit an offset from the test data which can be attributed to the integration method. The variation in the computed sectional loads due the LRTA and tunnel wall modeling at r/R =0.225 is larger than the revolution-to-revolution variation in the test data. Despite a more precise knowledge of the rotor trim loads and flow condition, the level of comparison between the computed and measured sectional airloads at $\mu = 0.37$ is comparable to the results shown in Ref. 3 for the high-speed flight test condition.

Figure 21 shows the sensitivity of the sectional airloads to the tab deflection for $\mu = 0.37$ at the outboard stations: r/R= 0.775, 0.865, and 0.920. (The stations inboard of r/R= 0.775 show no sensitivity to the tab deflection.) The comparison between computed and measured sectional normal force is slightly improved with the tab deflection. More significantly, the level of computed sectional pitching moment is very sensitive at r/R= 0.775 and 0.865 especially on the advancing side. This sensitivity is related to the strength and location of the normal shock that develops outboard on the advancing side of the rotor. The deflection of the tab causes small changes in the camber of the local airfoil section that alter the strength and location of the advancing blade shock. At $r/R = 0.775$, the tab deflection shifts the shock location on the upper surface from just forward of the quarter chord to just aft of the quarter chord which changes the computed pitching moment from negative to positive in the first quadrant. At r/R= 0.865 and 0.920, the tab deflection causes a shift in the shock location, but the change is not sufficient to explain the discrepancies between the computed sectional pressures and test data. Given the effects of the trim tab deflections on the sectional pitching moment for this advance ratio, the impact on sectional airloads at the other advance ratios should be investigated.

CONCLUDING REMARKS

Simulations of the UH-60A airloads rotor in the NFAC facility were made with the FUN3D unstructured-grid RANS CFD code loosely-coupled to the CAMRAD-II CSD code. To examine the influence of the test stand and wind-tunnel walls on the rotor performance and airloads, computations of the rotor installed on the NFAC Large Rotor Test Apparatus (LRTA) in free air and in the 40- by 80-ft wind tunnel were shown. Rotor trim tab deflections were also included in the CFD model to show the influence on performance and airloads. Computational results were shown for wind-tunnel test conditions corresponding to a speed sweep at constant lift up to an advance ratio of 0.40. Detailed comparisons were made between the results of the CFD/CSD simulations and a variety of the wind

tunnel measurements: rotor trim loads and trim control angles, rotor performance loads, rotor sectional loads, and blade pressures. The following observations can be made based on the results of the current computational study:

(1) The computed trends in solidity-weighted propulsive force and power coefficient matched the experimental trends over the range of advance ratios and are comparable to previously published results. Rotor performance and sectional airloads showed little sensitivity to the modeling of the wind-tunnel walls which indicates that the shaft angle correction adequately compensates for the wall influence up to an advance ratio of $\mu = 0.37$.

(2) Sensitivity of the rotor performance and sectional airloads to the modeling of the rotor with the LRTA body/hub increased with advance ratio. The inclusion of the LRTA in the CFD model slightly improved the comparison of rotor propulsive force between the computation and wind tunnel data but did not resolve the difference in the rotor power predictions at $\mu = 0.37$.

(3) The trim tab imparts a nose-up pitching moment to the rotor blade outboard on the advancing side of the rotor and increases the normal force on the tip of the rotor. The sensitivity of the pitching moment is related to the strength and location of the normal shock that develops outboard on the advancing side of the rotor.

(4) The computed sectional chord force results compared more favorably with measured data when a consistent integration method was used between the CFD and test. The computed sectional normal force and pitching moment were not sensitive to the integration method except in the case where a small number of pressure transducers were used in the integration.

(5) A comparison of unsteady pressure distributions showed differences in computed shock strength and position relative to test data at $\mu = 0.37$. The computed shock location on the advancing side of the rotor is forward of and slightly weaker than in the test data. Similar differences have been noted in CFD/CSD comparisons to the UH-60A Airloads high-speed flight test data.

(6) Despite a more precise knowledge of the rotor trim loads and flight condition, the level of comparison between the computed and measured sectional airloads at $\mu = 0.37$ is comparable to the results previously published for the high-speed flight test condition.

ACKNOWLEDGMENTS

REFERENCES

[1] Kufeld, R. M., Balough, D. L., Cross, J. L., Studebaker, K. F., Jennison, C. D., and Bousman, W. G., "Flight Testing of the UH-60A Airloads Aircraft," American Helicopter Society 50th Annual Forum Proceedings, 1994.

[2] Bousman, W. G. and Kufeld, R. M., "UH-60A Airloads Catalog," NASA TM 2005-212827, August 2005.

[3] Biedron, R. and Lee-Rausch, E., "Computation of UH-60A Airloads Using CFD/CSD Coupling On Unstructured Meshes," American Helicopter Society 67th Annual Forum Proceedings, 2011.

[4] Sankaran, V., Potsdam, M., Wissink, A., Datta, A., Jayaraman, B., and Sitaraman, J., "Rotor Loads Prediction in Level and Maneuvering Flight Using Unstructured-Adaptive Cartesian CFD," American Helicopter Society 67th Annual Forum Proceedings, 2011.

[5] Chaderjian, N. M. and Ahmad, J. U., "Detached Eddy Simulation of the UH-60 Rotor Wake Using Adaptive Mesh Refinement," American Helicopter Society 68th Annual Forum Proceedings, 2012.

[6] Biedron, R. T. and Lee-Rausch, E. M., "An Examination of Unsteady Airloads on a UH-60A Rotor: Computation versus Measurement," American Helicopter Society 68th Annual Forum Proceedings, 2012.

[7] Norman, T., Peterson, R., Shinoda, P., and Datta, A., "Full-Scale Wind Tunnel Test of the UH-60A Airloads Rotor," American Helicopter Society 67th Annual Forum Proceedings, 2011.

[8] Romander, E., Norman, T., and Chang, I.-C., "Correlating CFD Simulations with Wind Tunnel Test for the Full-Scale UH-60A Airloads Rotor," American Helicopter Society 67th Annual Forum Proceedings, 2011.

[9] Abrego, A. I., Olson, L. E., Romander, E. A., Barrow, D. A., and Burner, A. W., "Blade Displacement Measurement Technique Applied to a Full-Scale Rotor Test," American Helicopter Society 68th Annual Forum Proceedings, 2012.

[10] Yeo, H. and Romander, E., "Loads Correlation of a Full-Scale UH-60A Airloads Rotor in a Wind Tunnel," American Helicopter Society 68th Annual Forum Proceedings, 2012.

[11] Chang, I.-C., , Norman, T., and Romander, E., "Airloads Correlation of the UH-60A Rotor Inside the 40- by 80-Foot Wind Tunnel," AIAA Paper 2013-0636, January 2013.

[12] Marpu, R. P., Sankar, L. N., Norman, T. R., Egold, T. A., and Makinen, S., "Analysis of the UH-60A Rotor Loads Using Wind Tunnel Data," AIAA Paper 2013-0635, January 2013.

[13]Norman, T., Private Communication, NASA Ames Research Center, Moffett Field, CA, December 2011.

[14]Anderson, W. K. and Bonhaus, D. L., "An Implicit Upwind Algorithm for Computing Turbulent Flows on Unstructured Grids," *Computers and Fluids*, Vol. 23, (1), 1994, pp. 1–22.

[15]Noack, R. W., "DiRTlib: A Library to Add an Overset Capability to Your Flow Solver," AIAA Paper 2005-5116, June 2005.

[16]Noack, R. W., Boger, D. A., Kunz, R. F., and Carrica, P. M., "SUGGAR++: An Improved General Overset Grid Assembly Capability," AIAA Paper 2009-3992, June 2009.

[17]Johnson, W., "Rotorcraft Aerodynamics Models for a Comprehensive Analysis," American Helicopter Society 54th Annual Forum Proceedings, 1998.

[18]Romander, E. A., "Improved Coupling for UH-60 Performance Prediction," UH-60 Airloads Workshop, University of Maryland, August 2011.

[19]Prizadeh, S., "Three-Dimensional Unstructured Viscous Grids by the Advancing Front Method," *AIAA Journal*, Vol. 34, (1), January 1996, pp. 43–49.

[20]Bousman, W., Private Communication, U.S. Army Aeroflightdynamics, Moffett Field, CA, May 2011.
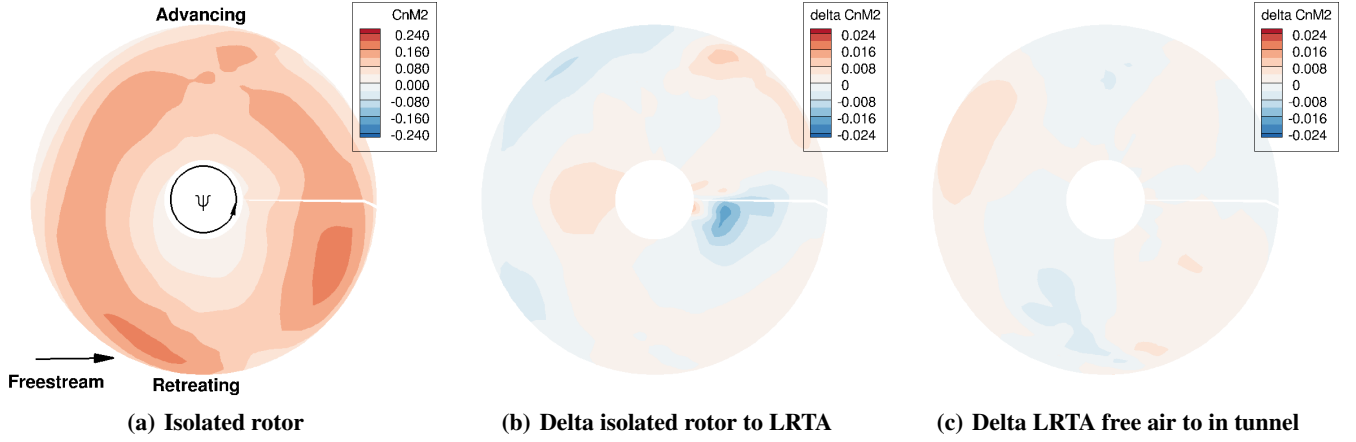
Fig. 7. Polar plot of computed sectional normal force ($M^2 C_n$) for $\mu = 0.15$.
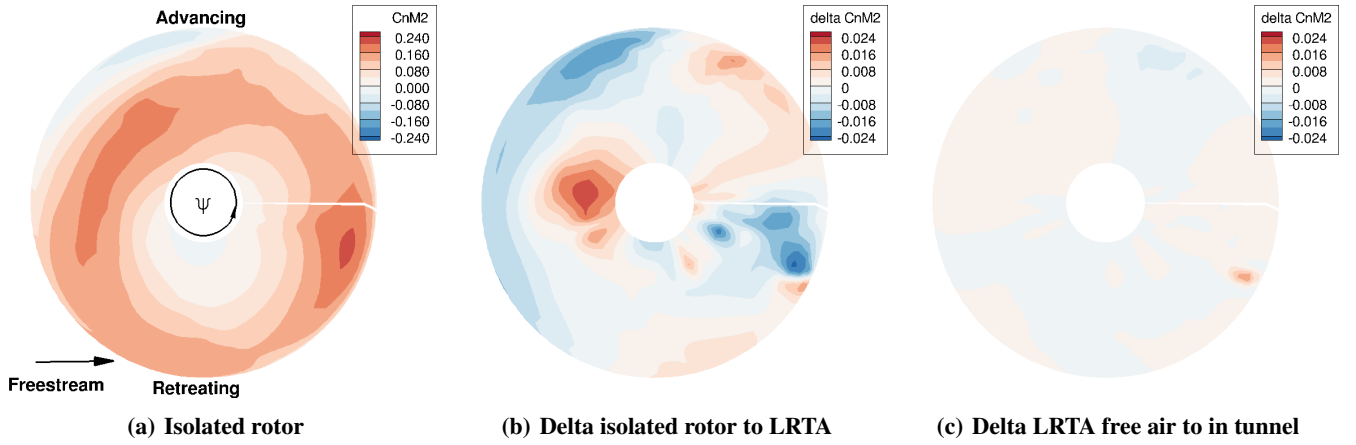
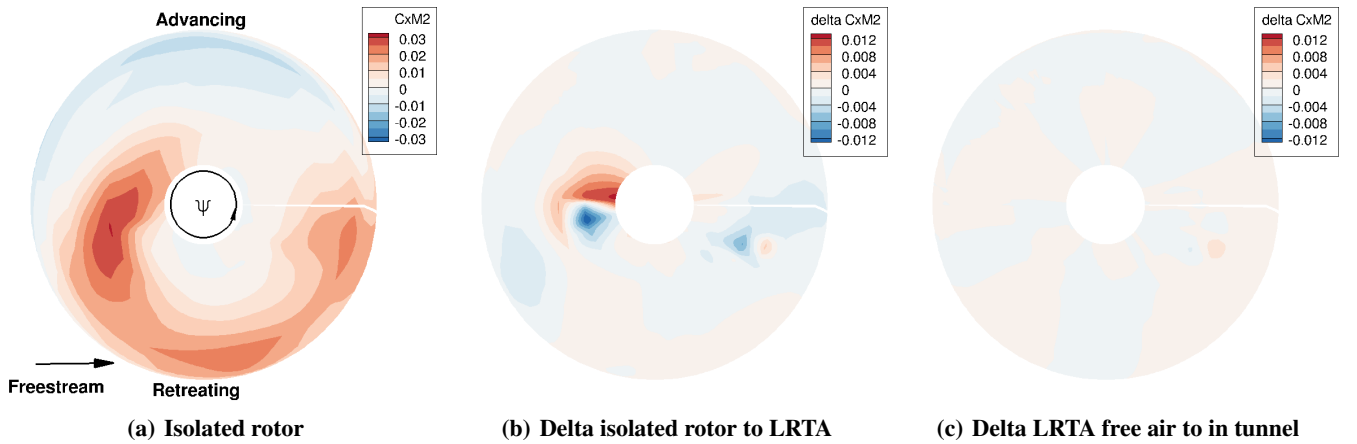**Fig. 8. Polar plot of computed sectional normal force ($M^2 C_n$) for $\mu = 0.30$.**
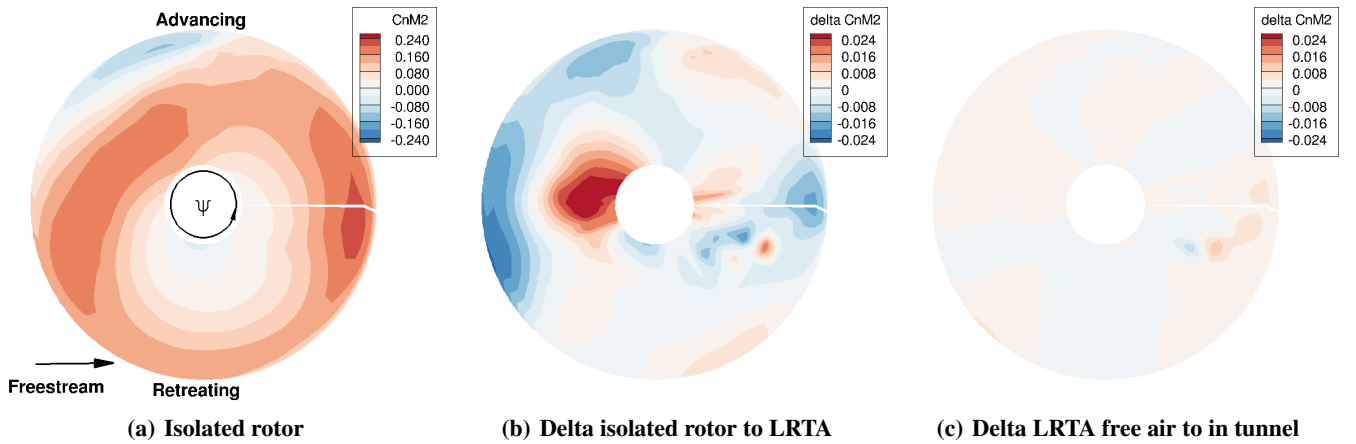
Fig. 9. Polar plot of computed sectional normal force ($M^2 C_n$) for $\mu = 0.37$.
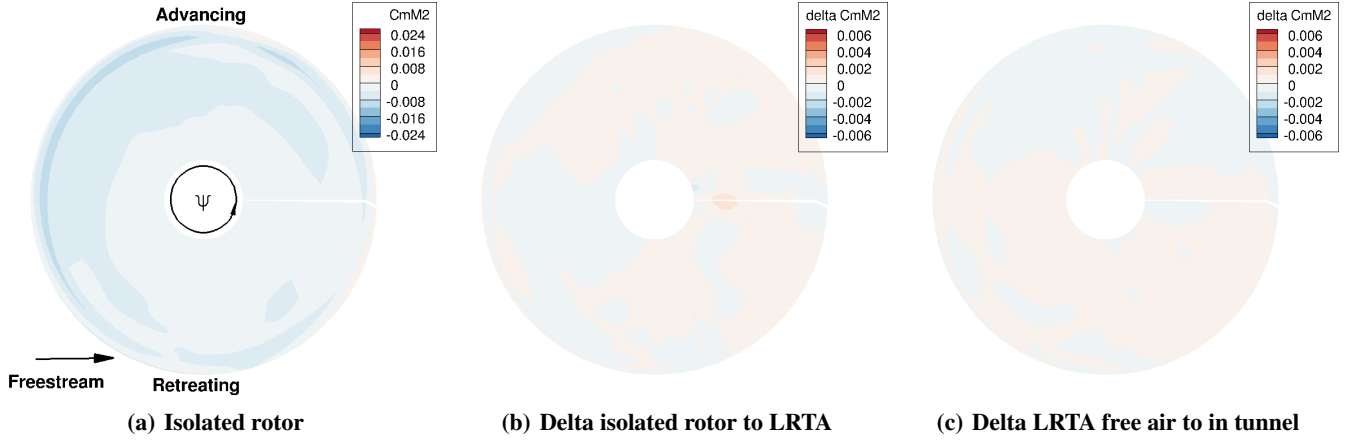
Fig. 10. Polar plot of computed sectional pitching moment (M^2C_m) for $\mu = 0.15$.
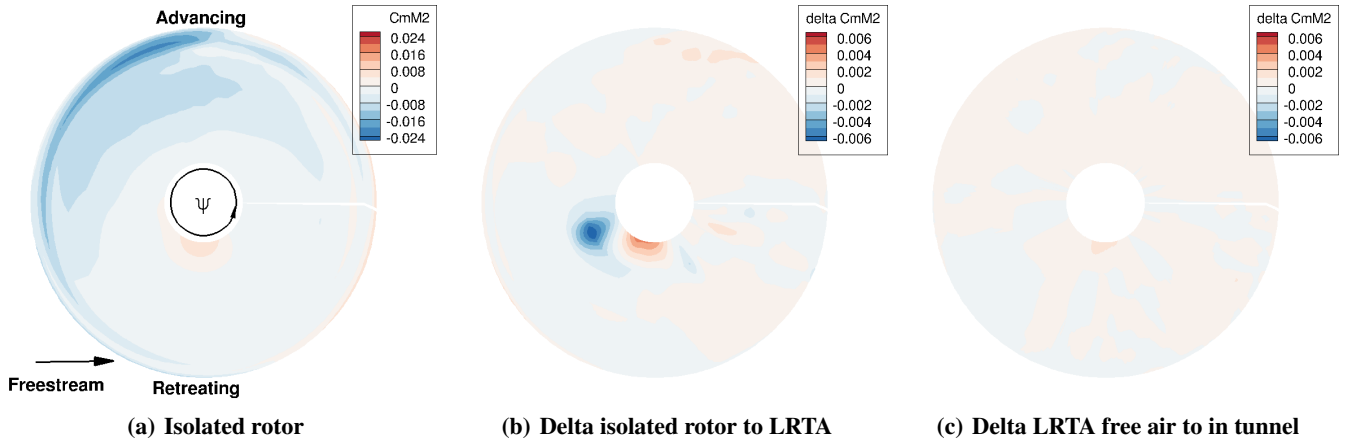
Fig. 11. Polar plot of computed sectional pitching moment (M^2C_m) for $\mu = 0.30$.
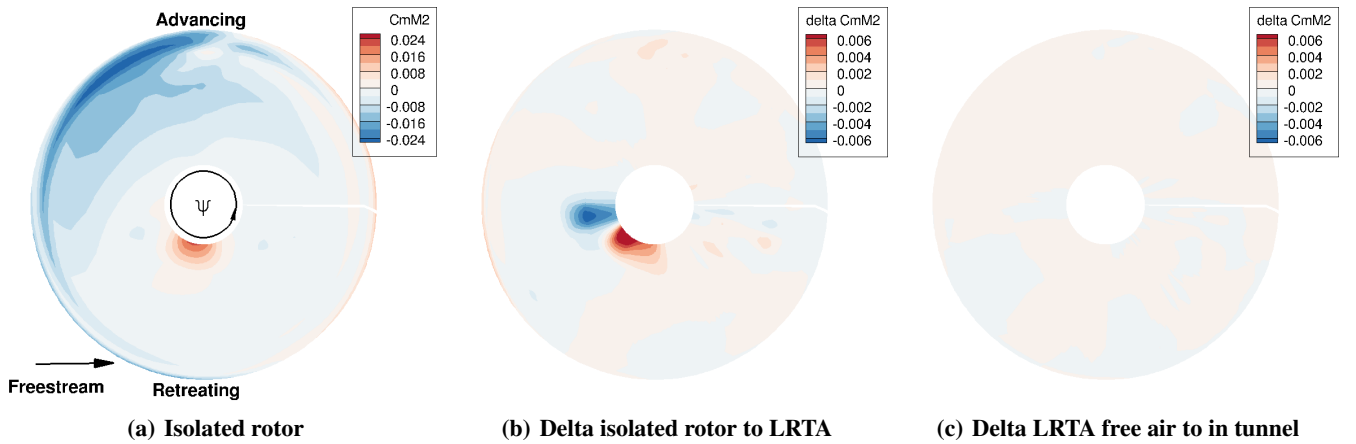
Fig. 12. Polar plot of computed sectional pitching moment (M^2C_m) for $\mu = 0.37$.
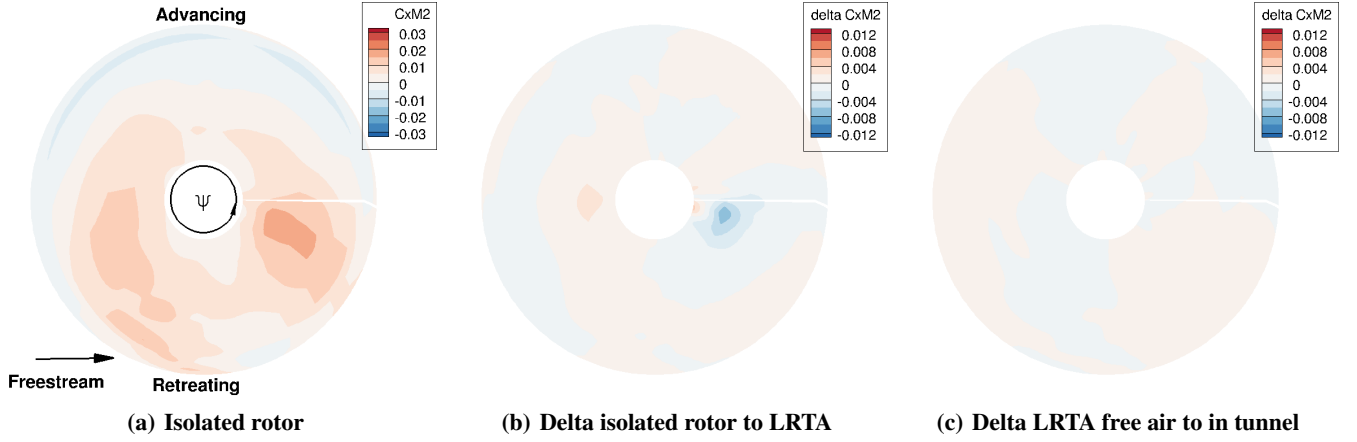
Fig. 13. Polar plot of computed sectional chord force ($M^2 C_c$) for $\mu = 0.15$.
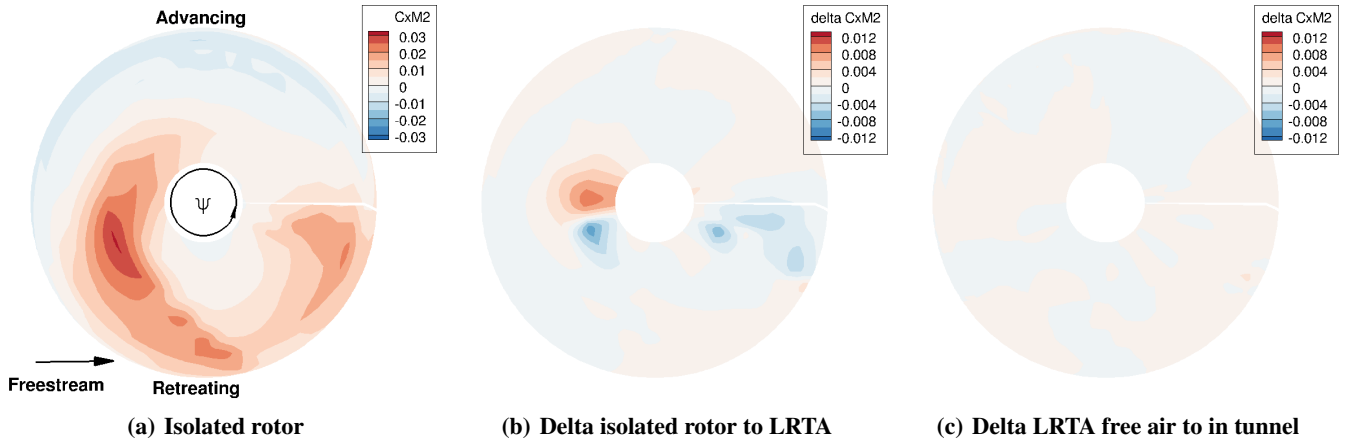
Fig. 14. Polar plot of computed sectional chord force ($M^2 C_c$) for $\mu = 0.30$.

Fig. 15. Polar plot of computed sectional chord force ($M^2 C_c$) for $\mu = 0.37$.

15

(a) Delta $M^2 C_n$ (b) Delta $M^2 C_m$ (c) Delta $M^2 C_c$
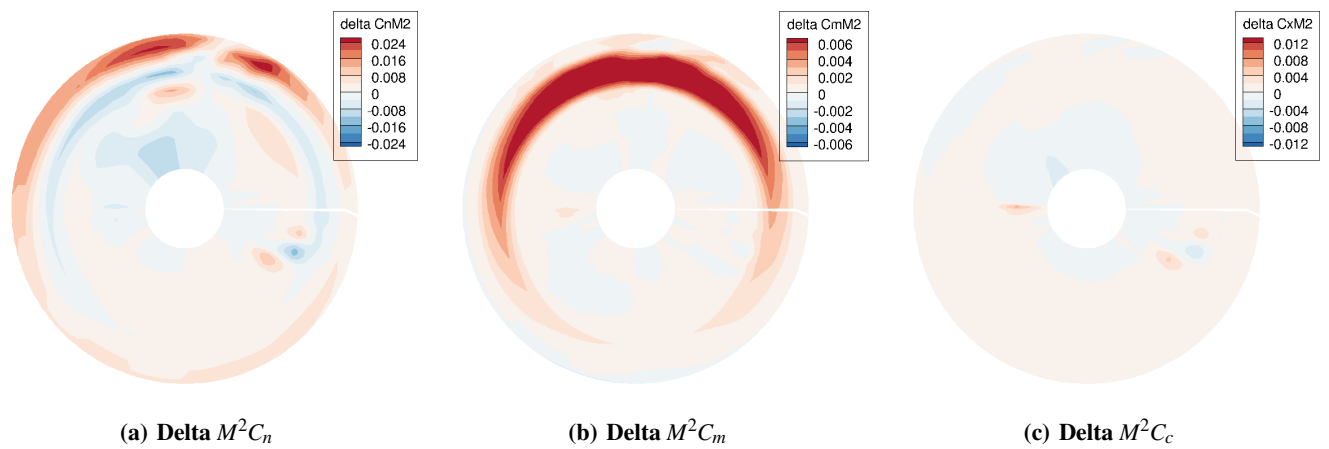
Fig. 16. Delta airloads from rotor/LRTA with nominal tab to deflected tabs for $\mu = 0.37$.
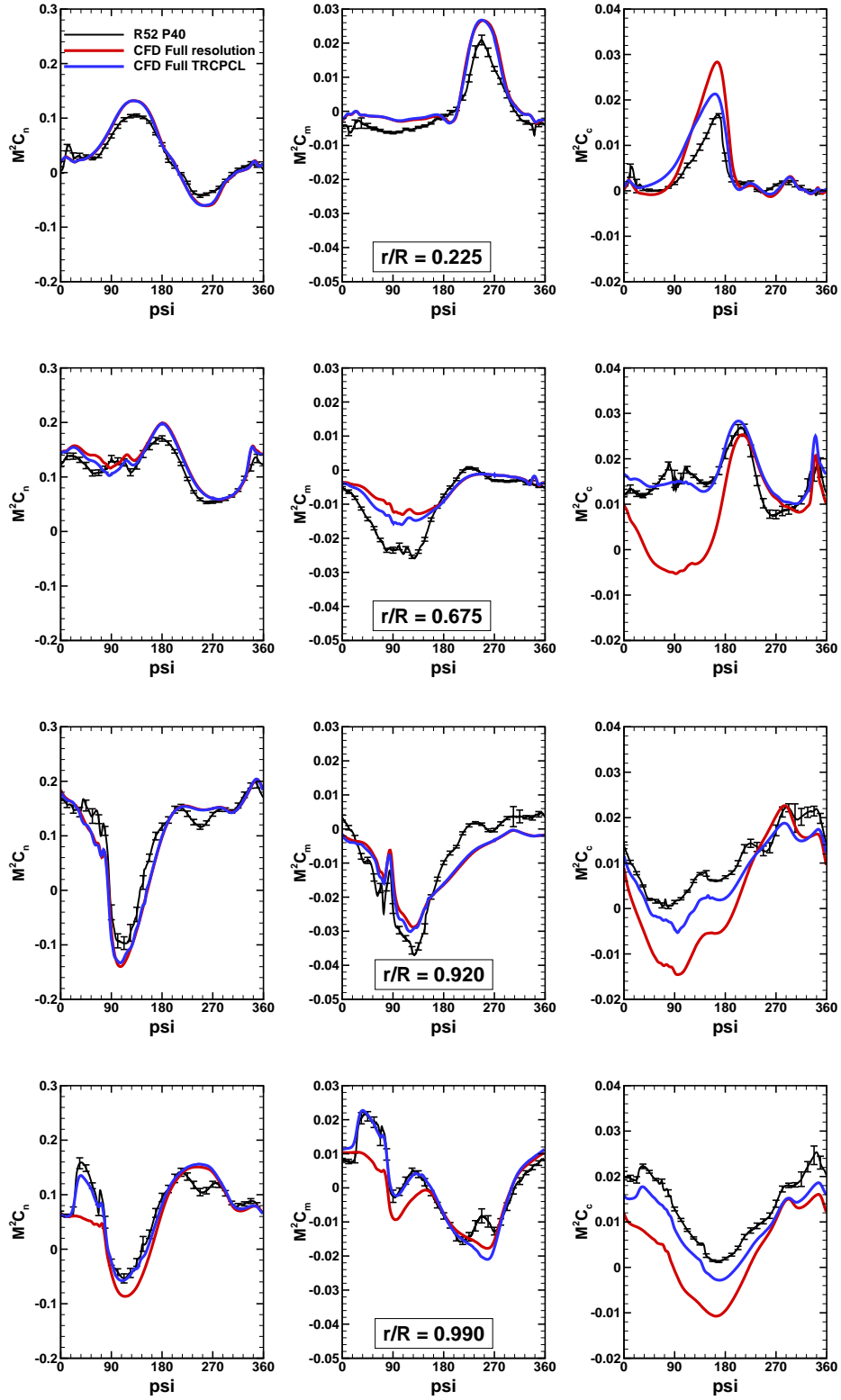
Fig. 17. Effect of integration method on CFD rotor/LRTA sectional forces and pitching moment for $\mu = 0.37$.
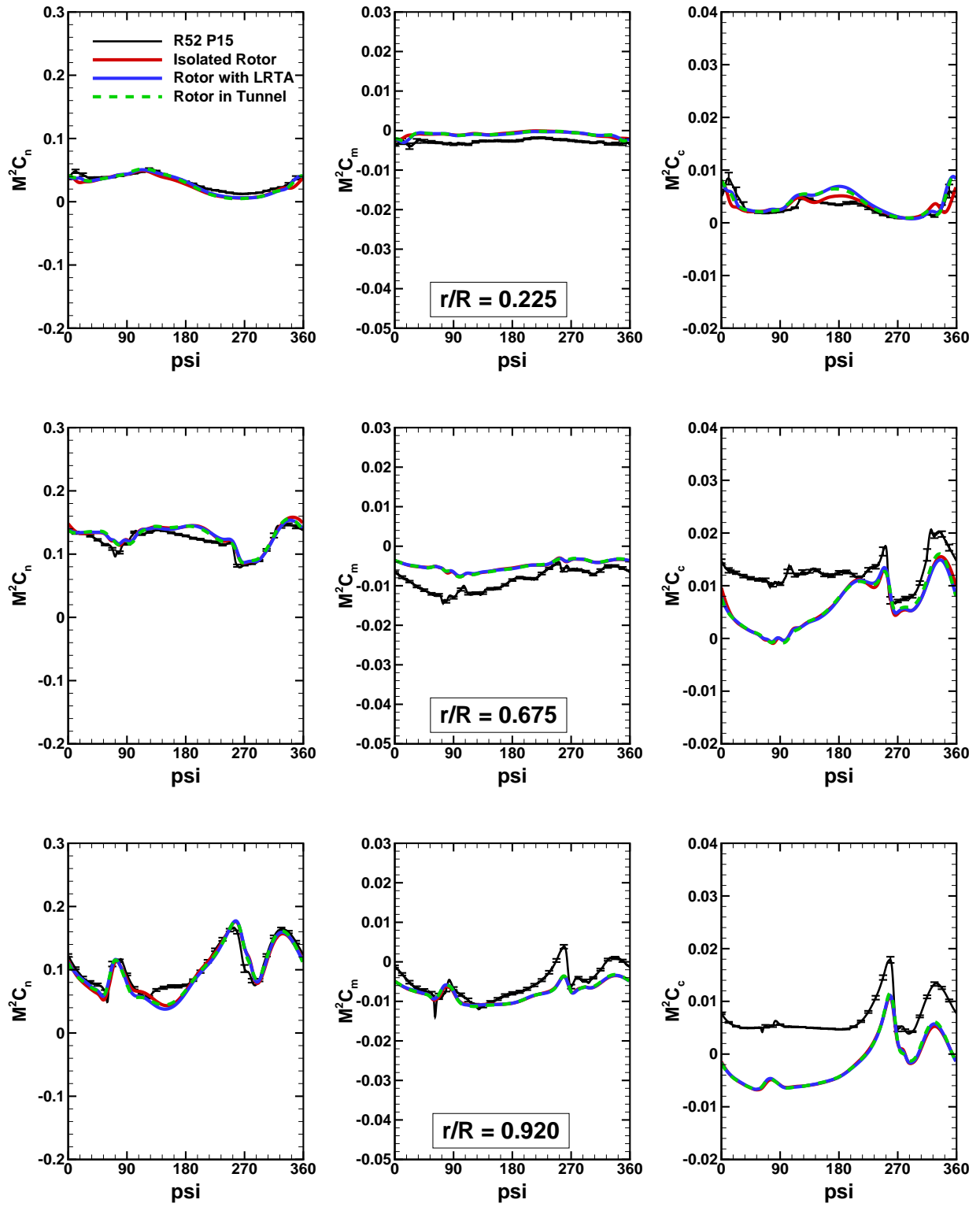
Fig. 18. Sectional forces and pitching moment for $\mu = 0.15$**.**
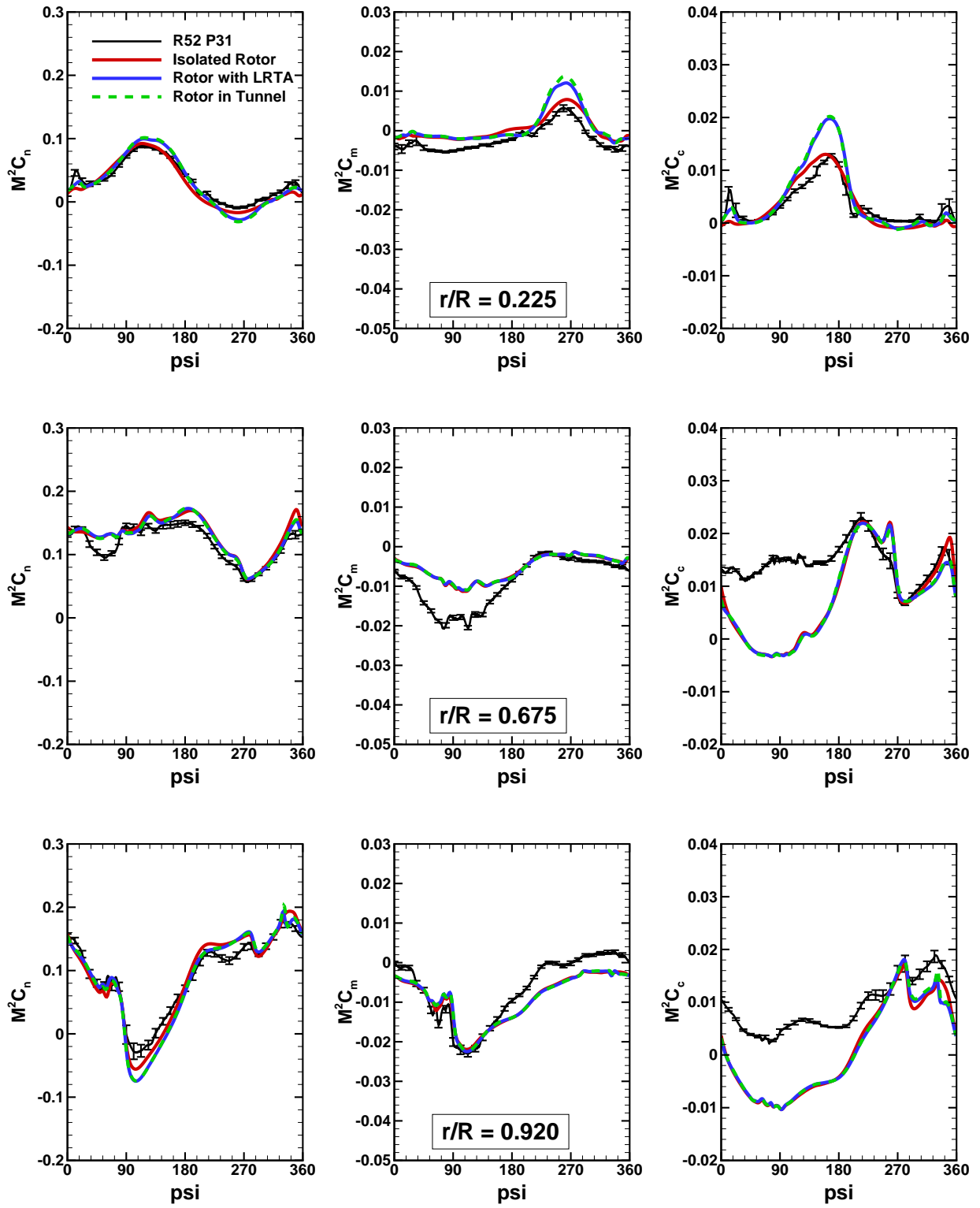
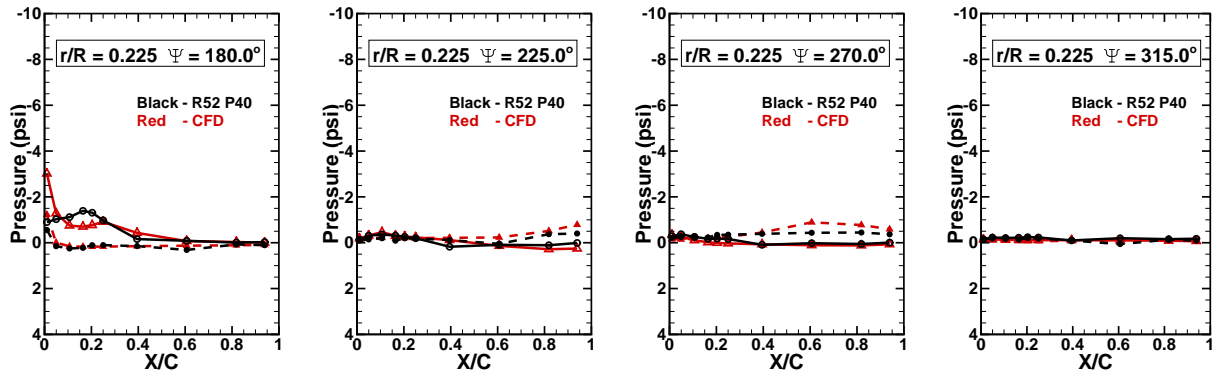**Fig. 19. Sectional forces and pitching moment for** $\mu = 0.30$**.**
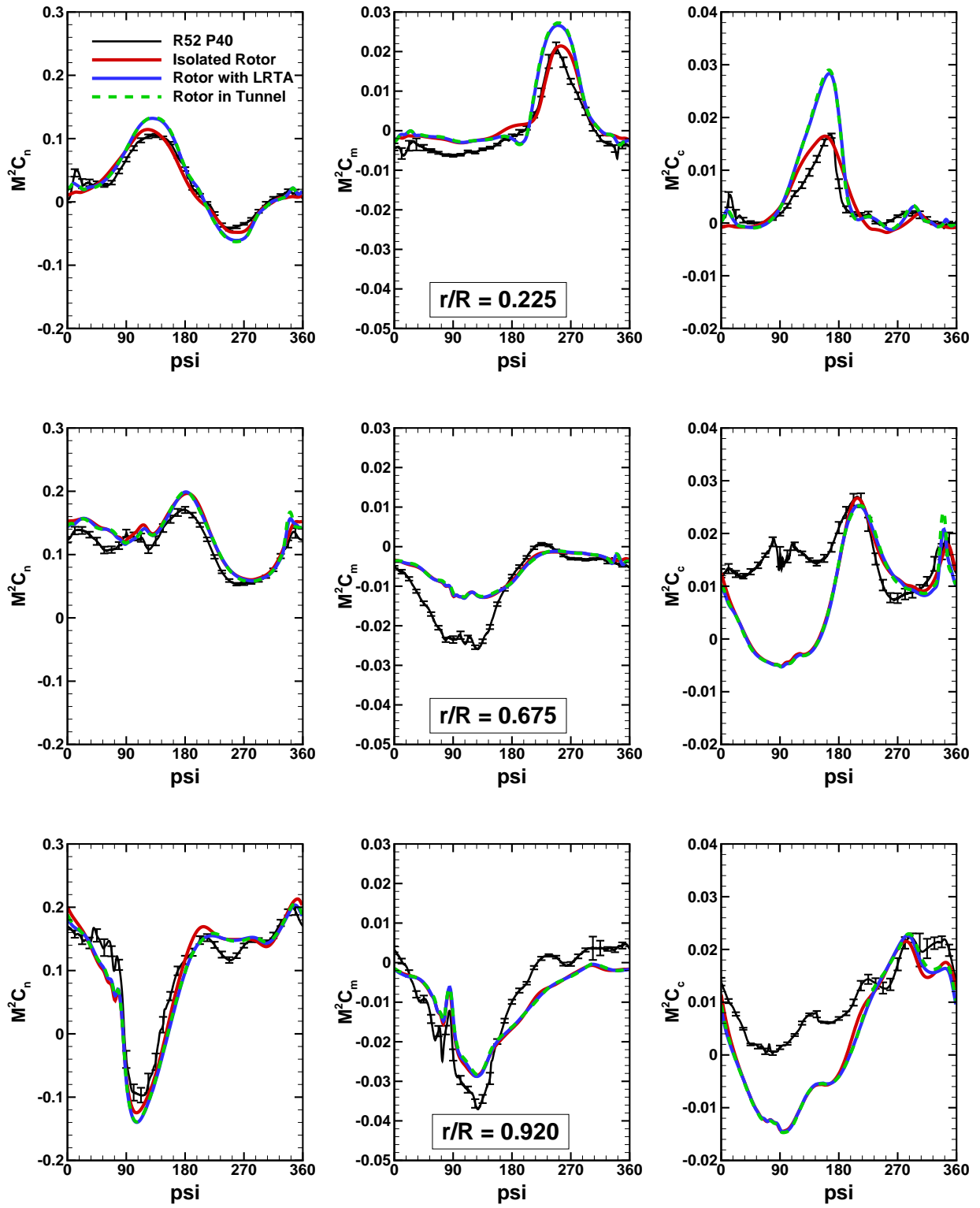
Fig. 20. Sectional forces and pitching moment for $\mu = 0.37$.
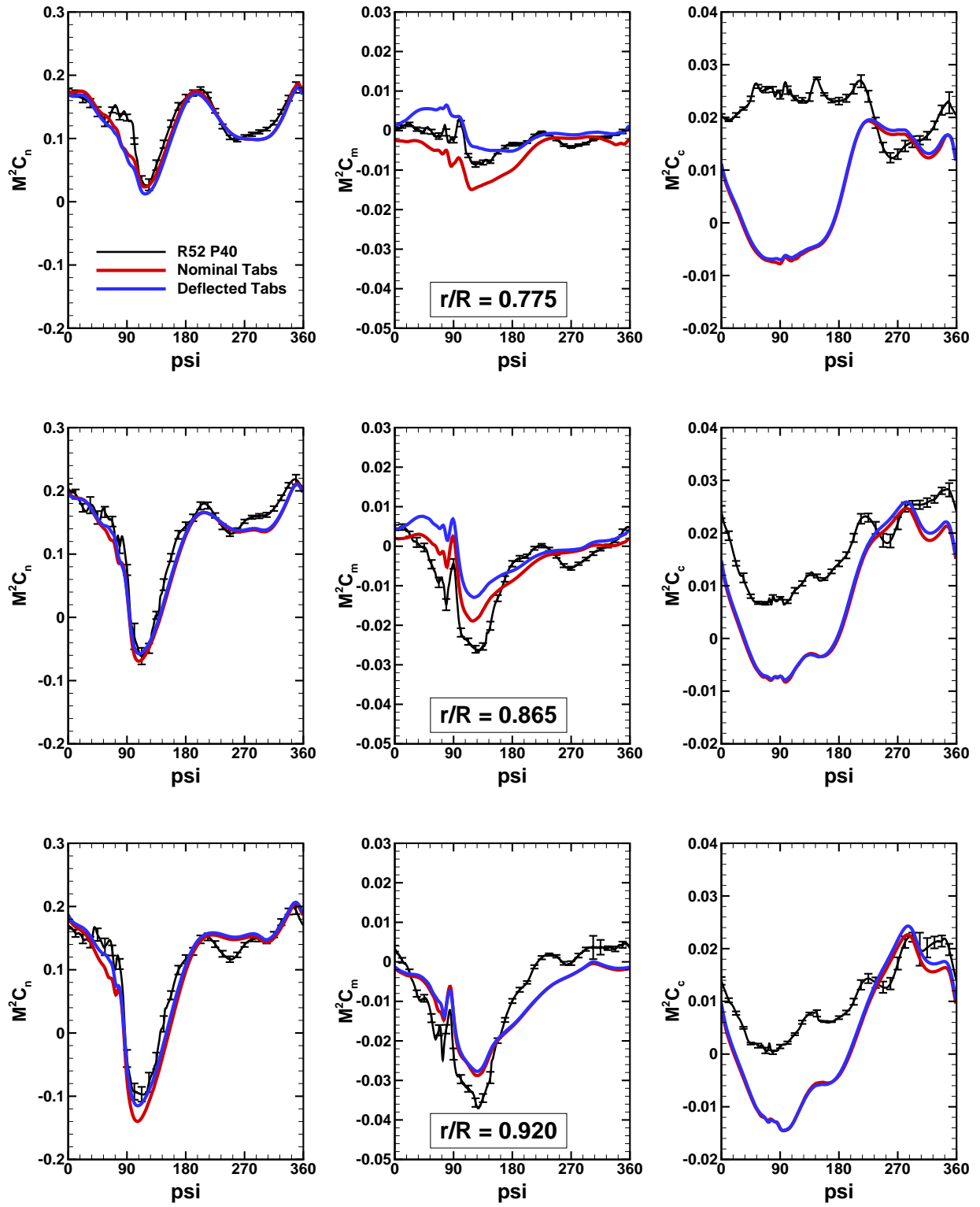
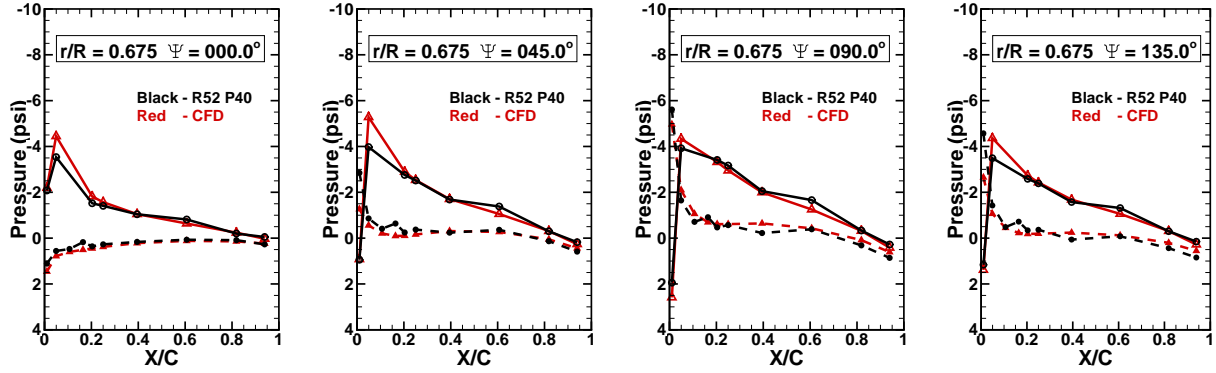**Fig. 21. Outboard sectional forces and pitching moment for** $\mu = 0.37$ **with deflected trim tabs.**
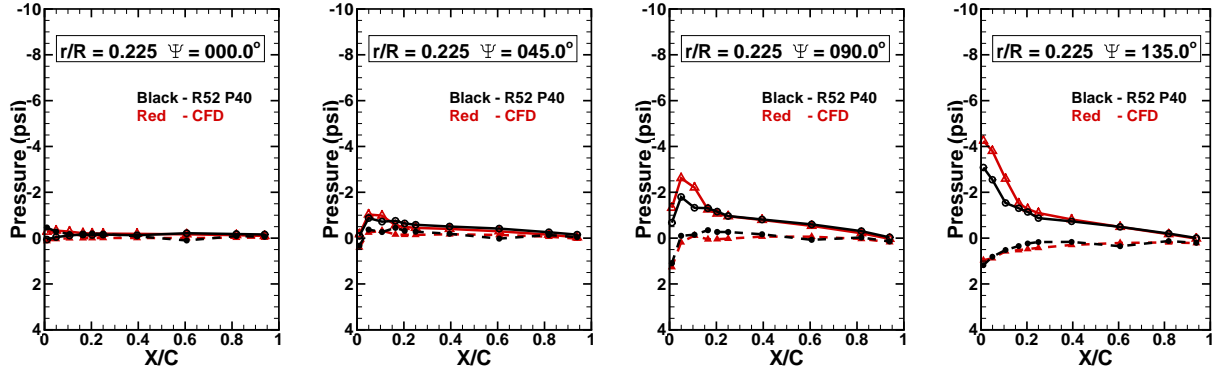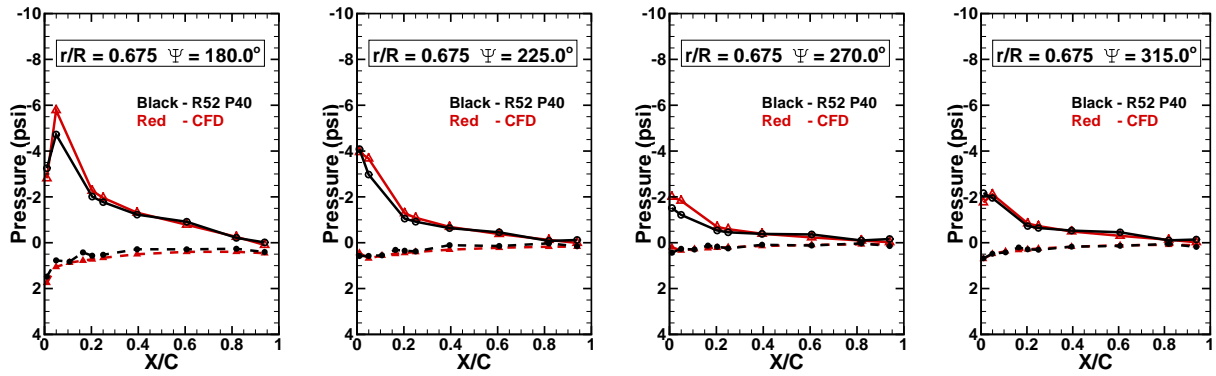
(a) Advancing side of $r/R = $ **0.225**

(b) Retreating side of $r/R = $ **0.225**

Fig. 22. Sectional pressures for the rotor with LRTA body/hub for $\mu = 0.37$ **(dashed lines–lower blade surface, solid lines–upper blade surface).**
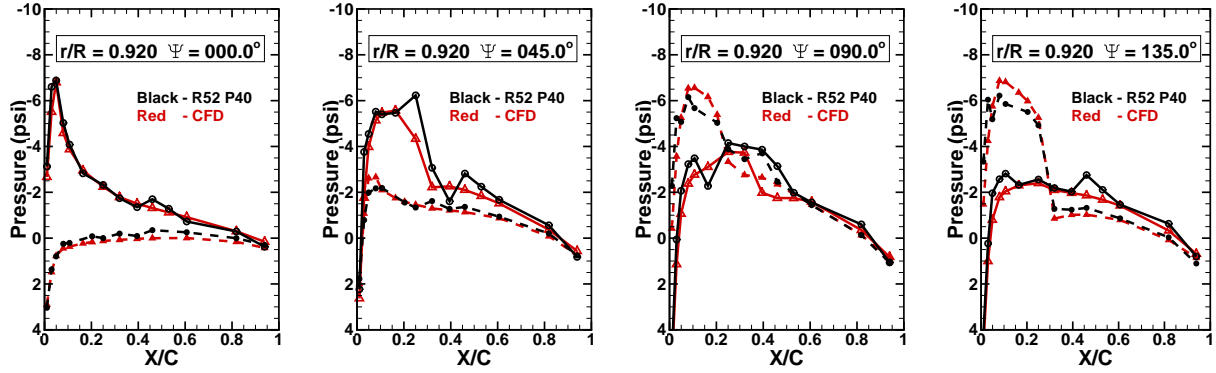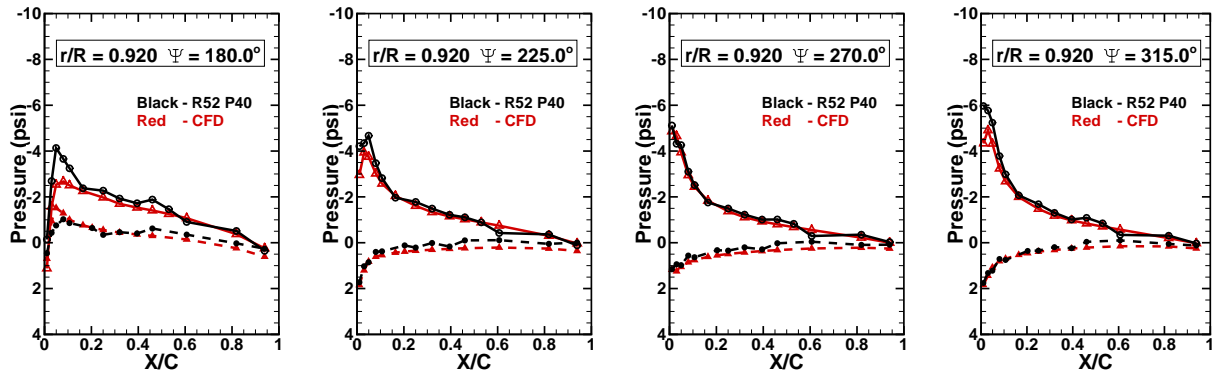
(a) Advancing side of $r/R =$ **0.675**

(b) Retreating side of $r/R =$ **0.675**

Fig. 23. Sectional pressures for the rotor with LRTA body/hub for $\mu = 0.37$ **(dashed lines–lower blade surface, solid lines–upper blade surface).**

(a) **Advancing side of** $r/R = 0.920$

(b) **Retreating side of** $r/R = 0.920$

Fig. 24. Sectional pressures for the rotor with LRTA body/hub for $\mu = 0.37$ **(dashed lines–lower blade surface, solid lines–upper blade surface).**